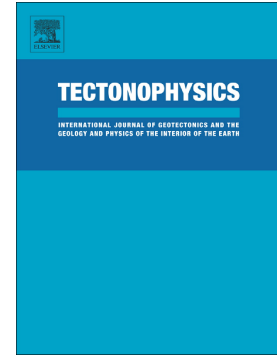# Accepted Manuscript

Crustal plumbing system of post-rift magmatism in the northern margin of South China Sea: New insights from integrated seismology

Shaohong Xia, Fang Zhao, Dapeng Zhao, Chaoyan Fan, Shiguo Wu, Lijun Mi, Jinlong Sun, Jinghe Cao, Kuiyuan Wan

Please cite this article as: Shaohong Xia, Fang Zhao, Dapeng Zhao, Chaoyan Fan, Shiguo Wu, Lijun Mi, Jinlong Sun, Jinghe Cao, Kuiyuan Wan , Crustal plumbing system of post-rift magmatism in the northern margin of South China Sea: New insights from integrated seismology. Tecto (2018), doi:10.1016/j.tecto.2018.07.002

Crustal plumbing system of post-rift magmatism in the northern margin of South China Sea: New insights from integrated seismology

Shaohong Xia[1, *], Fang Zhao[1], Dapeng Zhao[2], Chaoyan Fan[1], Shiguo Wu[3], Lijun Mi[4], Jinlong Sun[1], Jinghe Cao[1], Kuiyuan Wan[1]

1. *CAS Key Laboratory of Ocean and Marginal Sea Geology, South China Sea Institute of Oceanology, Chinese Academy of Sciences, Guangzhou, 510301, China*

2. *Department of Geophysics, Tohoku University, Sendai 980-8578, Japan*

3. *Institute of Deep-Sea Science and Engineering, Chinese Academy of Sciences, Sanya 572000, China*

4. *CNOOC Nanhai East Petroleum Bureau, Shenzhen, Guangdong 518054, China*

 * Corresponding Author: Shaohong Xia, Email: shxia@scsio.ac.cn

Highlights

- Revealing seismic features of post-rift magmatism in the SCS northern margin

- Lower crustal HVBs link to shallow igneous sills/intrusions and submarine volcanism

- The crustal plumbing system has a multilevel magmatic-transport mode

- Magma-poor SCS northern margin was rejuvenated by the Hainan mantle plume

Abstract

The origin and evolution of magmatism in rifting margins are a fundamental geological subject, and remain the focus of intense studies. Unlike the classical magma-poor and magma-rich rifting margins, the northern margin of the South China Sea (SCS) exhibits a strong post-rift magmatism, but the evolution and mechanism of this behavior are still poorly understood. In this work we investigate the detailed structural features of the post-rift magmatism in the crust of the SCS northern margin. Our analysis is based on wide-angle and multichannel reflection seismic data, combined with previous seismological results. Our results show a wide distribution of shallow igneous sills and intrusions. These features are spatially and tectonically linked to the lower crustal high-velocity bodies (HVBs) and submarine volcanism, indicating a causative connection between the three features. Considering the existence of an obvious low-velocity branch of the Hainan plume in the northern SCS and uplift of the lithosphere-asthenosphere boundary, we propose that the HVBs reflect consolidated mafic intrusions which formed the lower crustal reservoirs feeding the overlying igneous sills and intrusions. In the SCS northern margin where abundant extensional and detachment faults can act as magmatic channels, such a dynamic process might cause post-rift volcanism. Our results suggest that the crustal magmatic system of post-rift volcanism has a multilevel upward migration mode, and the HVBs in the lower crust could be the product of post-rift magmatism, further indicating that the SCS northern margin had a magma-poor property at the rifting phase but has undergone a strong magmatic rejuvenation by the subsequent mantle plume.

Keywords: Post-rift magmatism; South China Sea; Rifting margins; Sills; High-velocity bodies

1. Introduction

Rifted margins are generally classified into two end-members: magma-rich (volcanic) margins and magma-poor (non-volcanic) margins. Volcanic margins have some important features of vigorous magmatism in rifting and continental breakup, ultimately forming large volumes of intrusive and extrusive volcanic rocks, seaward-dipping reflectors from volcanic flows, and a high-velocity layer below the crust. The latter is related to magmatic underplating (e.g., White et al., 1989; Geoffroy, 2005; White and Smith, 2009; Keen et al., 2012). In contrast, non-volcanic margins are characterized by wide tracts of hyperextended crust, tilted fault blocks with listric normal faults, low-angle detachment faults in the brittle crust or upper mantle and possibly unroofed serpentinized mantle in the continent-ocean transition (e.g., Whitmarsh et al., 2001; Reston, 2009). Rifting and continental breakup might also depend on the complex interaction between stress, strain, temperature, and rheology (Ruppel, 1995).

As the largest and deepest marginal sea in the western Pacific Ocean, the South China Sea (SCS) has been a longtime study target in the Earth sciences (Nissen et al., 1995; Ding and Li, 2016; Sibuet et al., 2016). Unlike the classical magma-rich (e.g., Geoffroy, 2005; Keen et al., 2012) and magma-poor (e.g., Whitmarsh et al., 2001; Reston, 2009) rifting margins, the northern margin of the SCS has experienced unique tectonic processes from the late Mesozoic subduction of the Paleo-Pacific plate (Li and Li, 2007) to the Cenozoic rifting, with subsequent seafloor spreading (Li et al., 2014). These processes formed the distinct tectonism and magmatism landscape of the SCS northern margin (Franke et al., 2014; Fan et al., 2017). A number of extensional faults, which formed at the rifting stage, have been identified in the

3

northern SCS slope based on the multi-channel seismic profiles (e.g., Zhu et al., 2012). These extensional faults are closely related to the structural highs with igneous rocks, volcanic zones or tilted fault blocks in space (e.g., Gao et al., 2015). Although the magmatism was weak at the syn-rift and breakup stage of the northern SCS margin (Xu et al., 2012; Yan et al., 2014), the SCS has been replete with post-rift basaltic magmatism since the late Cenozoic, which is widely distributed throughout the region (Figure 1a; Hoang and Flower, 1998; Zhang et al., 2013; Yan et al., 2014; Zhao et al., 2016). Morphologically, plentiful post-rift submarine volcanism stands on the seafloor of the northern margin and oceanic basin (Zhao et al., 2014; Fan et al., 2017). As is well known, magmatism offers an important window into the deep Earth, assisting our understanding of various processes occurring in the Earth's lithosphere and mantle domain (Koppers and Watts, 2010). Hence, by studying the origin and nature of post-rift magmatism, we can better understand the deep geological processes beneath the SCS.

To date, most studies of the SCS submarine volcanoes have investigated their formation ages (Xu et al., 2012; Yan et al., 2014), shallow seismic structure (Sun et al., 2014; Zhao et al., 2016), and geochemical and petrological characteristics (Wang et al., 2012; Yan et al., 2015). Multichannel seismic data have confirmed plentiful submarine volcanoes in the SCS northern margin, which are characterized by high-amplitude reflection at their tops and frequent chaotic or disrupted internal seismic geometry that differs from that of the surrounding strata (Zhao et al., 2014; Fan et al., 2017). Igneous sills, intrusions and lava flows are common above or along the faults and fractures extending downwards to the deeper strata, indicating that the pre-existing faults and fractures provide preferential vertical pathways for the transfer of magma toward the surface (Sun et al., 2014; Zhao et al., 2016). As inferred from rock

samples and the stratigraphic contact relation on the multichannel seismic sections, almost all of the SCS submarine volcanoes formed in the post-rift periods (Yan et al., 2014; Zhao et al., 2016), indicating lack of strong magmatism in the rifting and breakup stages (Xu et al., 2012; Yan et al., 2014). The SCS northern margin also contains tilted fault blocks and wide tracts of hyperextended continental crust (Lester et al., 2014; Lei and Ren, 2016). Similar features appear in the Iberia magma-poor margin (e.g., Perez-Gussinye, 2013; Brune et al., 2017).

Given the weak magmatism at the rifting and breakup stages, why is the post-rift volcanism so unexpectedly extensive? Many researchers have suggested that a mantle plume might be responsible for the late Cenozoic basaltic magmatism and submarine volcanism in the SCS region (Xu et al., 2012; Yan et al., 2014; Xia et al., 2016; Fan et al., 2017). This inference was based on the OIB-like composition (e.g., Xu et al., 2012; Yan et al., 2014), as well as global and regional tomographic images (e.g., Zhao, 2007; Xia et al., 2016). However, how the magmatic system from the mantle formed crustal reservoirs and induced shallow volcanism in the SCS region remains unclear. Previous wide-angle seismic profiles (Figure 1b) have revealed the wide-ranging presence of high-velocity bodies (HVBs) in the lowermost crust of the SCS northern margin, which exhibit P-wave velocities of 7.0–7.6 km/s (Nissen et al., 1995; Yan et al., 2001; Wang et al., 2006; Zhao et al., 2010). Whether these HVBs are pre-rift relict mafic bodies (e.g., Nissen et al., 1995) or magmatic intrusions in the late Cenozoic (e.g., Yan et al., 2001; Wang et al., 2006; Zhao et al., 2010) is currently debated.

Clarifying or disproving a direct link between the HVBs in the lowermost crust and the post-rift volcanism in the SCS northern margin is pivotal to answering these remaining questions. In this work, we study the crustal structure and shallow igneous

sill complexes across the post-rift volcanism in the SCS northern margin using wide-angle seismic data obtained in 2014 and multichannel seismic profiles. We investigate the spatial and tectonic relationship between the HVBs in the lowermost crust, the overlying igneous sills and intrusions, and the submarine volcanism. Based on the present findings and previous results, we propose a multilevel upward magma transport model on the crustal plumbing system of the post-rift magmatism.

2. Data and Methods

2.1. Wide-angle seismic experiment and Data

In 2014, a new wide-angle seismic profile (Figure 1c) with a length of about 315 km was acquired with a seismic source comprising four equally sized (1500 inch^3) airguns with a total volume of 6000 inch^3. The source had a dominant frequency of 4-8 Hz, 3-5 wave peaks, and an amplitude of ±0.15 μm/s (Zhao et al., 2008). A total of 965 shots were fired with an interval of 120 seconds. The speed of the ship during the shooting was about 5-6 knots. The shot time and position were controlled with the bolt gun controller and a global positioning system (GPS), respectively. Fifteen ocean-bottom seismometers (OBSs), comprising one hydrophone and three-component geophones with a frequency of 2-100 Hz, were deployed with an interval of 15–20 km. The sampling rate of the OBSs in this experiment was 100. Unfortunately, two of the instruments were recovered without usable data and one was lost. In total, 965 shots were fired along the profile, and the synchronous single-channel section was also obtained. Each OBS was timing-corrected to account for clock drift, based on the GPS time synchronization that was performed before and after the OBS deployment. The position of each station on the seafloor was relocated by detecting direct water waves. We set the first shot at the northwestern end of this profile as the zero point. The location and distance of every shot and OBS were

calculated relative to the zero point in the model. The synchronous single-channel section was also converted to the zero point. The average offset of the OBSs in relation to the profile was about 0.07 km, and the largest offset was about 0.5 km. The offline OBSs are projected on the profile (Figures 2 and 4).

On the seismic record sections (Figure 2), we picked up arrival times of the intra-crustal refracted phases (Pg) and the reflected waves at the Moho discontinuity (PmP). It is possible that there are some other intra-crustal reflected phases, but it is very hard to distinguish these later phases because of the low signal-to-noise ratio. We have also found Pn phases in this study, but they are quite few, because the Pn phases only appear at large epicentral distances (> 100 km), whereas the energy of our seismic source was limited. In addition, the Pn phases in our OBS records are not very clear. Therefore, we did not pick up the fuzzy Pn phases to avoid adding more uncertainties to the inversion result. Finally, a total of 3474 Pg and 1490 PmP arrival times are collected. The picking accuracy of the Pg and PmP phases is estimated to be 50–80 ms and 70–100 ms, respectively. The shallow structure, revealed from the multichannel seismic data, approximately overlaps with our present wide-angle seismic profile (Figure 1c). We also collected data from many multichannel reflection seismic profiles to investigate the distribution of sills and intrusions in the study area (Figure 1b). These multi-channel (2D) seismic data are provided by the China National Offshore Oil Corporation (CNOOC) (Figs. 1, 5, 8 and 9), which were acquired from 576 channels with a shot-point spacing of 37.5 m and a common midpoint spacing of 12.5 m. The interpreted seismic profiles were imaged in IHS Kingdom[®] 8.7.

2.2. Method

A travel-time tomographic inversion method (tomo2d; Korenaga et al., 2000) is

used to jointly invert the arrival times of the refracted and reflected phases. This method can simultaneously determine a 2-D velocity model and the Moho geometry. Theoretical travel times and ray paths are calculated using a hybrid ray-tracing scheme based on the graph method and local ray-bending refinement. Our objective is to find an optimal velocity model that best satisfies the picked travel times within the limits of data accuracy.

Based on the single-channel seismic profile data obtained during the survey, the seafloor topography in the forward model is gridded with a spacing of 500 m. We constructed a starting velocity model by referring to the previous crustal models (Yan et al., 2001; Wang et al., 2006; Lester et al., 2014) obtained from the wide-angle seismic profiles (Figure 1b). We first read the depths of velocity contours from the previous results. Then the initial model is constructed by interpolating these depth values according to the general tectonic orientation. In contrast, the velocity values in our initial model are continuous in the crust but the velocity gradient varies with depth. To better constrain the structure of the sedimentary cover, we used both synchronous single channel and nearby multichannel seismic data to obtain the morphology of the sedimentary cover and basement. We used the drilling data from LF35-1-1 (Zhang et al., 2014) and the seismic velocities calculated from the Ps and secondary Pg phases (Wan et al. 2017) to do time-depth conversion. The horizontal cell size of the velocity field is 500 m, and the vertical cell size is 50 m and increases to 250 m at 30 km depth. We tested various combinations of the vertical and horizontal correlation lengths for the velocity nodes, as well as the smoothing and damping parameters. In the final model, the horizontal correlation length is 2 km at the top and 5 km at the bottom of the model. The corresponding vertical correlation lengths are 0.2 km and 0.5 km, respectively. The smoothing (damping) values for the

8

velocity and depth are set to be 150 (10) and 5 (40), respectively. In the inversion procedure, the depth-kernel weighting factor is set to be 0.5. After ten iterations, the observed and calculated travel times are well fitted (Figure 3a-3b). Compared with the initial model, the travel-time residuals for the final model have been greatly reduced, and more than 95% of the residuals are smaller than 0.1 s (Figure 3c-3d). The root-mean-square travel-time residual for the final crustal model is reduced to 85 ms, close to the data picking accuracy as mentioned above.

3. Results and Resolution Analysis

The optimal crustal velocity model obtained is shown in Figure 4. In general, the crustal thickness gradually thins from the shelf to the ocean basin, displaying a typical stretching characteristic of the rifted margin. This result is consistent with the previous models (Yan et al., 2001; Wang et al., 2006; Lester et al., 2014). A prominent feature is the existence of obvious HVBs in the lower crust with P-wave velocities of 7.0-7.6 km/s, showing a strong change in thickness along the section. Four high-velocity anomalous bodies are revealed (labeled H1–H4 in Figure 4b), which have a thickness of ~5–10 km and a variable length of ~20–50 km. The crustal structure exhibits considerable lateral variations along the profile. The HVBs exhibit convex shapes in the lower crust, and the velocities in the upper crust above H2 and H4 are relatively high (Figure 4b). There are also inclined high-V anomalies in the upper crust of the flank of H1 and H3. These convex HVBs are likely related to the intrusive dense sill complexes in the upper crust revealed by multichannel seismic data (Figure 5). Meanwhile, there is a close spatial consistency between the convex HVBs in the lower crust and the submarine mounds and shallow uplift as shown in Figure 4. To evaluate the validity of the final velocity model, we converted the seismic velocity to density using the Vp-ρ relation (Hamilton, 1978; Christensen and

9

Mooney, 1995). The free-air gravity anomaly along the profile is calculated using the MASK system (Yao et al., 2003). The gravity data are obtained from the global data base with a resolution of 1 min × 1 min (Sandwell et al., 2013). The HVBs are considered to be high-density bodies, and the calculated and observed gravity anomalies are well correlated (Figure 6). The HVBs correspond well to the peaks of the gravity anomalies (Figure 6).

The spatial resolution of our crustal model is evaluated by conducting a checkerboard resolution test (Figure 7). The main purpose of this test is to assess the adequacy of the ray coverage and to evaluate whether our data are capable of restoring a given model. The Moho depth is fixed in the test, and we find that this does not affect the test results. First, a checkerboard velocity model is made by assigning positive and negative velocity anomalies (±5%) to the grid nodes with a grid interval of 20 km x 7.5 km, and synthetic travel times are calculated for the checkerboard model. Then the synthetic data are inverted by using the same algorithm applied to the real data. The resolution is considered to be good for the areas where the checkerboard pattern is recovered. The inversion results show that the resolution is generally good in most parts of the crust (Figure 7c). Besides the checkerboard pattern, the amplitudes of velocity anomalies are also well recovered except in the edge portions. To demonstrate the reliability of the HVBs in the lower crust, we also conducted a restoring synthetic test (Figure 7d and 7e). The pattern and amplitudes of the input high-velocity anomalies in the lower crust are well recovered, suggesting that the HVBs are reliable features. In addition, we generated 100 randomized initial models with different crustal velocities and Moho depths to evaluate the effect of the initial model on the inversion results. The mean deviation of the 100 inverted models (Figure 8) provides a statistical measure of the velocity and Moho depth uncertainties

with the initial model (Korenaga et al., 2000). The results (Figure 8) show that the Moho depth uncertainty is about 1-1.5 km, and the velocity uncertainty is generally less than 0.1 km/s, and up to 0.2 km/s in only some local areas due to the sparse ray coverage, indicating that the final solution depends only slightly on the initial model chosen, and the velocity and Moho depth can be resolved within the uncertainty bounds.

To ascertain whether the submarine mounds were formed by volcanism, we analyzed the multichannel seismic section that roughly overlaps the crustal profile. The results are presented in Figure 5. The three obvious volcanic mounds (labeled V1–V3 in Figure 5a) show typical seismic features of igneous mounds revealed by a previous study (Zhao et al., 2014), namely, high-amplitude reflection at their tops and relatively weak internal seismic geometry. Dredged basalts from the submarine mounds in the northern SCS also evidence the post-rift submarine volcanism (Wang et al., 2012; Yan et al., 2015). We observed many high-amplitude reflections in the sedimentary layer, which may reflect three structural features: (1) carbonate sediments (e.g., Wu et al., 2014), (2) sandstone intrusions (e.g., Huuse and Mickelson, 2004), and (3) igneous sills (e.g., Hansen and Cartwright, 2006). The carbonate sediments often occur as thick and extensive biogenic constructions at some stage, controlled by a combination of tectonics, eustasy, oceanography and climatic conditions (Bachtel et al., 2003; Wu et al., 2014). The high-amplitude reflections described here have a relatively small-scale lateral extent. In addition, the abrupt lateral contact between high-amplitude anomalies and host strata is identified. The geometrical features and their distribution preclude the high-amplitude reflections with a carbonate origin. For the case of the sandstone intrusions, no evidence of sand remobilization in the northern SCS has been documented. In addition, sand

11

remobilization would be required for the expression of sandstone intrusions (Sun et al., 2014). However, there is no sandstone reservoir in the study area. In contrast, numerous igneous intrusive bodies in the northern SCS have been reported (e.g., Sun et al., 2014; Zhao et al., 2014), and igneous activity is also well known in the study area (e.g., Fan et al., 2017). The high-amplitude anomalies in the study area are similar in geometry and scale to the igneous sills documented in the SCS and in the Atlantic continental basins (e.g., Hansen and Cartwright, 2006; Jackson, 2012; Sun et al., 2014; Zhao et al., 2014). Meanwhile, a large-scale volcanism has been discovered adjacent to the igneous sills. The normal faults linked to the igneous sills likely formed vertical pathways facilitating the transfer of magma. All these pieces of evidence support the igneous origin for the high-amplitude anomalies in the study area.

The relatively high reliefs identified (Figure 5d) were induced by igneous intrusion-related strata uplift, as reported by previous studies (e.g., Jackson et al., 2013). These volcanic mounds and strata uplift are closely linked to the underlying shallow-level igneous sills and igneous intrusions, although being spatially offset by a few km (Figure 5), suggesting that the submarine volcanism was fed by magma from the sills via sub-vertical dikes along the pre-existing faults and fractures. The extensional faults seem to control the development and locations of the sills and dikes (Zhao et al., 2016). The size, frequency and intensity of volcanic eruptions are strongly controlled by the volume and connectivity of magmas within the crust (Kiser et al., 2016). In our results, the V1, V2, Dongsha Uplift and large-scale sill complexes clearly correspond to the larger anomalies H1 and H2, whereas the features of the strata uplift are related to the smaller anomaly H4. This relation suggests that the HVBs in the lower crust scale with the intensity of the shallow volcanic activity.

Hence, the HVBs are interpreted as the solidified crustal sources of the sills and dikes in the upper crust, and as the deep feeders of post-rift volcanism on the seafloor.

We systematically investigate the distribution of the sills and intrusions in the study area (Figure 9) based on the multichannel seismic profiles (Figure 1b). We find that the sills are widely developed and have a good correlation with the overlying volcanic bodies and lava flows (Figure 9). To better understand the correlation between the lower crustal HVBs, the sills and the submarine volcanism, we plot and compare the distribution maps of the lower crustal HVBs, sills and submarine volcanism in the study area (Figure 10). The distribution of the lower crustal HVBs is mainly based on the present result and the previous wide-angle seismic profiles (black lines in Figure 1b). We identify the sills (Figure 9) and ascertain their distribution (Figure 10) using the multichannel seismic data (gray lines in Figure 1b). Locations of the submarine volcanic mounds are from the detailed results of Fan et al. (2017). Figure 10 shows that the spatial distribution of the sills and the overlying volcanic mounds strikingly corresponds to the underlying HVBs in the lower crust of the slope area. The volcanic mounds are closely associated with the terminations of the highest points of the linked cuspate sills, although a sideways displacement of a few km exists between them (Figure 5). However, few similar features are visible in the shelf area on the left corner of Figure 10, which may be related to the thicker crust that hindered the rise of magma there.

4. Discussion

In this work prominent HVBs are revealed in the lower crust (Figure 4), which are generally consistent with the previous results (Yan et al., 2001; Wang et al., 2006; Zhao et al., 2010; Lester et al., 2014). A growing number of studies have reported magma-poor continental margin characteristics in the SCS northern margin, including

a wide hyperextended continental crust (Gao et al., 2015), tilted fault blocks that sole into a low-angle detachment (McIntosh et al., 2014; Lester et al., 2014), and listric normal faults (Zhu et al., 2012). Meanwhile, petrological studies have revealed that the magmatic activities in the SCS were very weak at the syn-rift stage (Xu et al., 2012; Yan et al., 2014). Hence, the HVBs in the lower crust cannot be magmatic products of the syn-rift phase. An uppermost mantle serpentinization source of the HVBs has also been ruled out by considering the crustal thickness and P- and S-wave velocities in the study area (Yan et al., 2001; Wang et al., 2006; Zhao et al., 2010; Gao et al., 2015). The HVBs cannot be pre-rift residual mafic rocks either, because their maximum P-wave velocity in South China and its coastal area is 7.0 km/s (Li et al., 2006; Zhang and Wang, 2007; Xia et al., 2010). It is well known that the SCS was formed by the extension of the Southern China block. So the lower crust beneath South China and its coastal area is considered as a normal lower crust with velocities lower than 7.0 km/s. The HVBs are defined with a P-wave velocity higher than 7.0 km/s in our study, and they are mainly located in the lowermost crust. Combining the extensive post-rift magmatic features with the volcanic evidence found in the shallow areas (e.g., sills, seamounts; Wang et al., 2012; Sun et al., 2014; Yan et al., 2015; Zhao et al., 2016), we deem that the HVBs in the lower crust most likely resulted from the post-rift magmatism (Zhao et al., 2010; Lester et al., 2014).

One striking feature of our results is the spatial relation between the HVBs in the lower crust and the overlying volcanic mounds (Figure 10). The lower crust beneath an active volcano usually has a clear low-velocity magma chamber supporting the volcanic activity (e.g., Xia et al., 2007; Huang et al., 2015; Zhao et al., 2018). When the volcanic activity ceases, the low-velocity magma chamber gradually cools, eventually becoming a residual high-velocity anomaly with a denser mafic

14

composition than the active chamber (Kiser et al., 2016). According to dated basaltic-rock samples from the seamounts and the stratigraphic contact relationship in the SCS northern margin (Wang et al., 2012; Yan et al., 2015; Zhao et al., 2016), most of the submarine volcanoes in our study area formed at ~8–22 Ma. Accordingly, the original hot magma reservoir in the lower crust, which supported the post-rift volcanism in the SCS northern margin, may have cooled completely and become a high-velocity feature. Hence, we interpret the HVBs in the lower crust as the cooled mafic intrusions and crustal magma reservoirs that once fed the post-rift volcanism.

One low-velocity branch of the Hainan plume is revealed in the upper mantle (Xia et al., 2016), which is located below the development zone of the lower crustal HVBs. Petrological results have shown that samples of the seamounts in the northern SCS have similar geochemical and petrological composition with the volcanic basalt in Hainan (e.g., Xu et al., 2012; Wang et al., 2012; Yan et al., 2014). Meanwhile, a sharp uplift of the lithosphere-asthenosphere boundary occurs just below the crustal HVBs (Figure 11). These lines of evidence suggest that the lower crustal HVBs as well as the strong post-rift magmatism in the SCS northern margin could be caused by the Hainan plume arising from the lower mantle.

Our results show the presence of sills, igneous intrusions, lava flows and tilted faults beneath the submarine volcanoes and strata uplift (Figures 5 and 9). These sills and lava flows might have fed the submarine volcanoes through the tilted faults which provide conduits. Zhao et al. (2014) carefully analyzed the relation between the volcanic mounts and the underlying igneous sills in the SCS northern margin, and suggested that igneous materials migrate upward along clear pipes or fault conduits from the sills to the overlying volcanoes. Similar shallow magmatic systems of ancient sill-fed submarine volcanoes were mapped in the Bight Basin and the Faroe–

Shetland Basin (Schofield and Totterdell, 2008; Jackson, 2012; Magee et al., 2013). Many magmatic sills were identified beneath an ultramafic-hosted hydrothermal system at depths of ~2–10 km, which reflect partially molten intrusions (Canales et al., 2017). Sun et al. (2014) also found many sills and igneous intrusions in the Miocene strata of the present study area, exhibiting discordant high-amplitude seismic anomalies with similar seismic features to our results (Figures 5 and 9). These studies indicate that sills provide an important link between the deep magma source and the surface volcanism. Therefore, the sills can be considered as the relay station of a magmatic plumbing system.

Previous studies have revealed a large number of extensional faults (Zhu et al., 2012) and detachment faults (Lester et al., 2014; McIntosh et al., 2014) in the northern SCS, which may have become effective channels for the later magma migration. Fan et al. (2017) calculated the basal elliptical major axes of 45 volcanic mounds, and found that strikes of these volcanic mounds are well consistent with the strike of extensional faults. They also suggested that the preexisting faults might provide magmatic conduits for the subsequent post-rift volcanism. Our results show that the magma sills are surrounded by a number of tilted faults (Figure 5), which may have provided feeding conduits. In this scenario, the sills and lava flows could form by the upward movement of deep magma through the conduits.

Figure 11 shows a schematic diagram illustrating the complex, multilevel magma transport in the crust during the intrusion and eruption events in the SCS northern margin, based on the present findings and previous results. Magmas ascending from the upper mantle intruded into the lower crust and accumulated to form crustal reservoirs. As the relay station of magma migration to the Earth's surface, these shallow intrusive igneous sill and intrusion complexes facilitated the vertical and

lateral transports of magma through the crust. The volcanic mounds accreted on the seabed, showing a sideways displacement of a few km with the tips of the basaltic sills and lava flows. Our results and the magmatic-migration scenario (Figure 11) are consistent with recent studies of subaerial volcanic systems with multilevel magmatic transport (Marjanovic et al., 2014; Canales et al., 2017). The HVBs in the lower crust are geographically linked to the post-rift volcanism, suggesting that they caused the post-rift magmatic intrusion. Previous teleseismic and surface-wave tomographic studies (Tang and Zheng, 2013; Xia et al., 2016) have indicated that the upper mantle conditions are suitable for the magmatic intrusion into the lower crust beneath the SCS region. It is highly possible that the strong post-rift magmatism in the SCS northern margin was associated with the Hainan plume arising from the deep mantle.

5. Conclusions

We present a new crustal velocity model by analyzing seismic reflection data along a transect of the post-rift submarine volcanoes in the SCS northern margin. Significant HVBs are revealed in the lower crust, which are spatially related to the surface geological features. These HVBs may reflect the consolidated intrusive magma sources of the shallow sills and post-rift volcanism in the margin. The volatile-rich and overheated melts from the lower crustal reservoirs may have ascended along the extensional faults or pre-existing weak zones through the thinned crust, then intruded into the shallow area to form the post-rift volcanism. The sills and lava flows revealed on the multichannel seismic sections may have acted as a relay station in the magmatic plumbing system. Combining our new findings with the previous results, we propose that the crustal plumbing system has a multilevel magmatic transport mode. Our results also confirm that the HVBs resulted from the post-rift magmatism, further evidencing the non-volcanic nature of the present

17

northern margin of the SCS but strong rejuvenation by the later post-rift magmatism.

Acknowledgements

References

Bachtel, S.L., Kissling, R.D., Martono, D., Rahardjanto, S.P., Dunn, P.A., MacDonald, B.A., 2003. Seismic stratigraphic evolution of the Miocene–Pliocene Segitiga Platform, East Natuna Sea, Indonesia: the origin, growth and demise of an isolated carbonate platform. In: Eberli, G.P., Massaferro, J.L., Sarg, J.F. (Eds.), Seismic Imaging of Carbonate Reservoir and Systems, 81. AAPG Memoir, Tulsa, pp. 309–328.

Barckhausen, U., Engels, M., Franke, D., Ladage, S., Pubellier, M., 2014. Evolution of the South China Sea: Revised ages for breakup and seafloor spreading. Mar. Petrol. Geol. 58, 599-611.

Brune, S., Heine, C., Clift, P., Perez-Gussinye, M., 2017. Rifted margin architecture and crustal rheology: Reviewing Iberia-Newfoundland, Central South Atlantic, and South China Sea. Mar. Petrol. Geol. 79, 257-281.

Canales, J., Dunn, R., Arai, R., Sohn, R., 2017. Seismic imaging of magma sills beneath an ultramafic-hosted hydrothermal system. Geology 45(5), 451-454.

Christensen, N., Mooney, W., 1995. Seismic velocity structure and composition of the continental crust: a global view. J. Geophys. Res. 100, 9761-9788.

Ding, W.W., Li, J.B., 2016. Propagated rifting in the Southwest Sub-basin, South China Sea: Insights from analogue modelling. J. Geodyn. 17, 71-86.

Fan, C., Xia, S., Zhao, F., Sun, J., Cao, J., Xu, H., Wan, K., 2017. New insights into the magmatism in the northern margin of the South China Sea: Spatial features and volume of intraplate seamounts. Geochem. Geophys. Geosyst. 18, doi:10.1002/2016GC06792.

Franke, D., Savva, D., Pubellier, M., Steuer, S., Mouly, B., Auxietre, J., Meresse, F., Rooke, N., 2014. The final rifting evolution in the South China Sea. Mar. Petrol. Geol. 58, 704-720.

Gao, J., Wu. S., McIntosh. K., Mi. L., Yao, B., Chen, Z., Jia, L., 2015. The continent-ocean transition at the mid-northern margin of the South China Sea. Tectonophys. 654, 1-19.

Geoffroy, L., 2005. Volcanic passive margins. C. R. Geoscience 337(16), 1395-1408.

Hamilton, E., 1978. Sound velocity-density relations in seafloor sediments and rocks. J. Acoust. Soc. Am. 63(2), 366-377.

Hansen, D.M., Cartwright, J.A., 2006. The three-dimensional geometry and growth of forced folds above saucer-shaped igneous sills. J. Struct. Geol. 28, 1520–1535.

Hoang, N., Flower, M., 1998. Petrogenesis of Cenozoic basalts from Vietnam: Implication for origins of a diffuse igneous province. J. Petrol. 39(3), 369-395.

Huang, H., Lin, F., Schmandt, B., Farrell, J., Smith, R., Tsai, V., 2015. The Yellowstone magmatic system from the mantle plume to the upper crust. Science 348, 773-776.

Huuse, M., Mickelson, M., 2004. Eocene sandstone intrusions in the Tampen Spur area (Norwegian North Sea Quad 34) imaged by 3D seismic data. Mar. Petrol. Geol. 21, 141-155.

Jackson, C., 2012. Seismic reflection imaging and controls on the preservation of ancient sill-fed magmatic vents. J. Geol. Soc. London 169, 503-506.

Jackson, C., Schofield, N., Golenkov, B., 2013. Geometry and controls on the development of igneous sill-related forced folds: A 2-D seismic reflection case study from offshore southern Australia. Geol. Soc. Am. Bull. 125, 1874-1890.

Keen, C., Dickie, K., Dehler, S., 2012. The volcanic margins of the northern Labrador Sea: Insights to the rifting process. Tectonics 31, doi:10.1029/2011TC002985.

Kiser, E., Palomeras, I., Levander, A., Zelt, C., Harder, S., Schmandt, B., Hansen, S., Creager, K., Ulberg, C., 2016. Magma reservoirs from the upper crust to the Moho inferred from high-resolution Vp and Vs models beneath Mount St. Helens, Washington State, USA. Geology 44(6), 411-414.

Koppers, A., Watts, B., 2010. Intraplate seamounts as a window into deep earth processes. Oceanography 23(1), 42-57.

Korenaga, J., Holbrook, W., Kent, G., Kelemen, P., Detrick, R., Larsen, H., Hopper, J., Dahl-Jensen, T., 2000. Crustal structure of the southeast Greenland margin from

joint refraction and reflection seismic tomography. J. Geophys. Res. 105, 21591-21614, doi:10.1029/2000JB900188.

Lei, C., Ren, J., 2016. Hyper-extended rift systems in the Xisha Trough, northwestern South China Sea: Implications for extreme crustal thinning ahead of a propagating ocean. Mar. Petrol. Geol. 77, 846-864.

Lester, R., Avendonk, H., McIntosh, K., Lavier, L., Liu, C., Wang, T., Wu, F., 2014. Rifting and magmatism in the northeastern South China Sea from wide-angle tomography and seismic reflection imaging. J. Geophys. Res. 119, 2305-2323.

Li, C., Xu, X., Lin, J., Sun, Z., Zhu, J., et al., 2014. Ages and magnetic structure of the South China Sea constrained by deep tow magnetic surveys and IODP Expedition 349. Geochem. Geophys. Geosyst. 15, doi:10.1002/2014GC005567.

Li, S., Mooney, W.D., Fan, J., 2006. Crustal structure of mainland China from deep seismic sounding data. Tectonophys. 420, 239-252.

Li, Z., Li, X., 2007. Formation of the 1300-km-wide intracontinental orogen and postorogenic magmatic province in Mesozoic South China: A flat-slab subduction model. Geology 35(2), 179-182.

Magee, C., Hunt-Stewart, E., Jackson, C., 2013. Volcano growth mechanisms and the role of sub-volcanic intrusions: insights from 2D seismic reflection data. Earth Planet. Sci. Lett. 373, 41-53.

Marjanovic, M., Carbotte, S., Carton, H., Nedimovic, M., Mutter, J., Canales, J., 2014. A multi-sill magma plumbing system beneath the axis of the East Pacific Rise. Nature Geosci. 7, 825-829.

McIntosh, K., Lavier, L., Avendonk, H., Lester, R., Eakin, D., Liu, C., 2014. Crustal structure and inferred rifting processes in the northeast South China Sea. Mar Petrol. Geol. 58, 612-626.

Nissen, S.S., Hayes, D.E., Yao, B., Zeng, W., Chen, Y., Nu, X., 1995. Gravity, heat flow, and seismic constraints on the processes of crustal extension: northern margin of South China Sea. J. Geophys. Res. 100, 22447-22483.

Perez-Gussinye, M., 2013. A tectonic model for hyperextension at magma-poor rifted margins: an example from the West Iberia-Newfoundland conjugate margins. Geol. Soc. London Spec. Pub. 369, 403-427.

Reston, T.J., 2009. The structure, evolution and symmetry of the magma-poor rifted margins of the North and Central Atlantic: A synthesis. Tectonophysics, 468, 6-27.

Ruppel, C., 1995. Extensional processes in continental lithosphere. J. Geophys. Res. 100, 24187-24216.

Sandwell, D., Garcia, E., Soofi, K., Wessel, P., Smith, W., 2013. Towards 1 mGal global marine gravity from CryoSat-2, Envisat, and Jason-1, Leading Edge 32(8), 892, doi:10.1190/tle32080892.1.

Schofield, A., Totterdell, J., 2008. Distribution, timing and origin of magmatism in the Bight and Eucla Basins. Geosci. Austral. Record 24, 19.

Sibuet, J., Yeh, Y., Lee, C., 2016. Geodynamics of the South China Sea. Tectonophys. 692, 98-119.

Sun, Q., Wu, S., Cartwright, J., Wang, S., Lu, Y., Chen, D., Dong, D., 2014. Neogene igneous intrusions in the northern South China Sea: Evidence from high-resolution three dimensional seismic data. Mar. Petrol. Geol. 54, 83-95.

Tang, Q., Zheng, C., 2013. Crust and upper mantle structure and its tectonic implications in the South China Sea and adjacent regions. J. Asian Earth Sci. 62, 510-525.

Wan, K., Xia, S., Cao, J., Sun, J., Xu, H., 2017. Deep seismic structure of the northern South China Sea: Origin of a high-velocity layer in the lower crust. J. Geophys. Res. 122, doi:10.1002/2016JB013481.

Wang, K., Lo, Y., Chung, S., Lo, C., Hsu, S., Yang, H., Shinjo, R., 2012, Age and geochemical features of dredged basalts from offshore SW Taiwan: The coincidence of Intra-Plate magmatism with the spreading South China Sea. Terres. Atmos. Ocean. Sci. 23(6), 657-669.

Wang, T.K., Chen, M., Lee, C., Xia, K., 2006. Seismic imaging of the transitional crust across the northeastern margin of the South China Sea. Tectonophys. 412, 237-254.

Wessel, P., Smith, W., 1998. New, improved version of the Genetic Mapping Tools released. EOS Trans. Am. Geophys. Un. 79, 579.

White, R., McKenzie, D., 1989. Magmatism at rift zone: the generation of volcanic continental margins and flood basalts. J. Geophys. Res. 94, 7685-7729.

White, R., Smith, L., 2009. Crustal structure of the Hatton and the conjugate east Greenland rifted volcanic continental margins, NE Atlantic. J. Geophys. Res. 114, B02305, doi:10.1029/2008JB005856.

Whitmarsh, R.B., Manatschal, G., Minshull, T.A., 2001. Evolution of magma-poor continental margins from rifting to seafloor spreading. Nature 413, 150-154.

Wu, S., Yang, Z., Wang, D., Lü, F., Lüdmann, T., Fulthorpe, C., Wang, B., 2014. Architecture, development and geological control of the Xisha carbonate platforms, northwestern South China Sea. Mar. Geol. 350, 71–83.

Xia, S., Zhao, D., Qiu, X., Nakajima, J., Matsuzawa, T., Hasegawa, A., 2007. Mapping the crustal structure under active volcanoes in central Tohoku, Japan

using P and PmP data. Geophys. Res. Lett. 34, L10309, doi:10.1029/2007GL030026.

Xia, S., Zhao, M., Qiu, X., Xu, H., Shi, X., 2010. Crustal structure in an onshore-offshore transitional zone near Hong Kong, northern South China Sea. J. Asian Earth Sci. 37, 460-472.

Xia, S., Zhao, D., Sun, J., Huang, H., 2016. Teleseismic imaging of the mantle beneath southernmost China: New insights into the Hainan plume. Gondwana Res. 36, 33-43.

Xu, Y., Wei, J., Qiu, H., Zhang, H., Huang, X., 2012. Opening and evolution of the South China Sea constrained by studies on volcanic rocks: Preliminary results and a research design. Chin. Sci. Bull. 57, 3150-3164.

Yao. C., Hao, T., Guang, Z., Zhang, L., 2003. High-speed computation and efficient storage in 3-D gravity and magnetic inversion based on genetic algorithms. Chin. J. Geophys. 46, 252-258.

Yan, P., Zhou, D., Liu, Z., 2001. A crustal structure profile across the northern continental margin of the South China Sea. Tectonophys. 338, 1-21.

Yan, Q., Shi, X., Castillo, P., 2014. The late Mesozoic-Cenozoic tectonic evolution of the South China Sea: A petrologic perspective. J. Asian Earth Sci. 85, 178-201.

Yan, Q., Castillo, P., Shi, X., Wang, L., Liao, L., Ren, J., 2015. Geochemistry and petrogenesis of volcanic rocks from Daimao Seamount (South China Sea) and their tectonic implications. Lithos 218-219, 117-126.

Zhang, B., Wang, P., Zhang, G., Sun, X., Lu, B., Ni, W., 2013. Cenozoic volcanic rocks in the Pearl River Mouth and Southeast Hainan Basins of South China Sea and their implications for petroleum geology. Petrol. Explor. Develop. 40(6), 704-713.

Zhang, Z., Wang, Y., 2007. Crustal structure and contact relationship revealed from deep seismic sounding data in South China. Phys. Earth Planet. Inter. 165, 114-126.

Zhang, L., Zhang, G., Wang, L., 2014. The distribution of Mesozoic sedimentary in the northern South China Sea and the prospect of oil and gas resources. Pp.197-201, Beijing: Geological Publishing House.

Zhao, D., 2007. Seismic images under 60 hotspots: search for mantle plumes. Gondwana Res. 12, 335-355.

Zhao, D., Liu, X., Hua, Y., 2018. Tottori earthquakes and Daisen volcano: Effects of fluids, slab melting and hot mantle upwelling. Earth Planet. Sci. Lett. 485, 121-129.

Zhao, M., Qiu, X., Xia, S., Wang, P., Xu, H., Ye, C., Kang, Y., 2008. Large volume air-gun sources and its seismic waveform characters. Chin. J. Geophys. 51, 558-565 (in Chinese).

Zhao, M., Qiu, X., Xia, S., Xu, H., Wang, P., Wang, T., Lee, C., Xia, K., 2010. Seismic structure in the northeastern South China Sea: S-wave velocity and V_p/V_s ratios derived from the three-component OBS data. Tectonophys. 480, 183-197.

Zhao, F., Wu, S., Sun, Q., Huuse, M., Li, W., Wang, Z., 2014. Submarine volcanic mounds in the Pearl River Mouth Basin, northern South China Sea. Mar. Geol. 355, 162-172.

Zhao, F., Alves, T., Wu, S., Li, W., Huuse, M., Mi, L., Sun, Q., Ma, B., 2016. Prolonged post-rift magmatism on highly extended crust of divergent continental margins (Baiyun Sag, South China Sea). Earth Planet. Sci. Lett. 445, 79-91.

Zhu, J., Qiu, X., Kopp, H., Xu, H., Sun, Z., Ruan, A., Sun, J., Wei, X., 2012. Shallow anatomy of a continent-ocean transition zone in the northern South China Sea from multichannel seismic data. Tectonophys. 554-557, 18-29.

Figure 1. (a) Topography and bathymetry map of the South China Sea (SCS) with distribution of the late Cenozoic basaltic magmatism. The red shadows with age data display the basalt locations revealed by outcrops in the field, wells and dredged samples, etc. These data are from Tu et al. (1992), Hoang et al. (1998), Wang et al. (2012), Yan et al. (2014), and Zhao et al. (2016). The age data suggest the basaltic magmatism in the SCS should mainly occur in the post-rift to post-spreading periods. The orange ellipses denote the volcanic seamounts (Fan et al., 2017). The left-upper global map shows the SCS location. (b) Overview map of the study area. The pink line with circles denotes locations of our wide-angle seismic profile and ocean bottom seismometers (OBSs) used in this study. Black lines show locations of the previous wide-angle seismic profiles from which lower crustal HVBs were revealed. Gray lines show locations of multichannel reflection seismic data which are used to identify the sills and intrusions. Red short lines with a, b, c and d symbols denote locations of multichannel reflection seismic data shown in Figure 8, which are used to reveal the features of sills, volcanic bodies and lava flows. (c) Detailed location map showing our newly obtained data. The white line denotes the multichannel seismic section that approximately overlaps with our present wide-angle seismic profile. The pink line denotes the wide-angle seismic profile along which the shots were fired. The black dots show locations of 15 ocean bottom seismometers. V1, V2 and V3 denote locations of three submarine post-rift volcanoes identified from the multichannel seismic profiles shown in Figures 4 and 5. The white thick line (a, b) denotes the continent-ocean boundary (COB).

Figure 2. Seismic record sections with a reducing velocity of 6.0 km/s and 3-10 Hz

bandpass filter at (a) OBS03, (b) OBS07, (c) OBS10 and (d) OBS15. Pg denotes the refracted phase in the crust. PmP denotes the reflected phase from the Moho discontinuity.

Figure 3. (a) Comparison of observed (green) and calculated (red) travel times of the same phases for all of the receivers in the final model. (b) Travel-time residuals for the starting model (green) and the final model (red), indicating that the final velocity model greatly reduces the residuals. The final RMS travel-time residual is 85 ms. Histogram of the travel-time residuals for the initial velocity model (d) and the final velocity model (d).

Figure 4. (a) Single-channel seismic section synchronized with the wide-angle seismic profile, bathymetry map along the wide-angle seismic profile and locations of the ocean bottom seismometers (orange circles), submarine post-rift volcanoes (V1-V3, red large arrows), and forced folds induced by igneous intrusions (F1-F2, red thin arrows). (b) The final crustal velocity model derived from the wide-angle seismic data. H1-H4 denotes high-velocity bodies (HVBs) in the lower crust, which are spatially associated with the shallow volcanism and forced folds.

Figure 5. (a) A multichannel seismic section approximately overlapping the crustal profile. V1, V2 and V3 show clear seismic features of volcanic mounds. F1 and F2 mark locations of strata uplifts by igneous intrusions. Sills, dikes and faults are visible beneath the volcanic mounds. The black boxes denote locations of Figure 5b-5d. (b) Detailed seismic image beneath the left flank of site V1. The sills and dikes complexes are clearly visible. (c) Enlarged seismic image beneath the right flank of site V2. The sills, dikes, lava flows and faults have a larger scale and they are spatially correlated. (d) Enlarged picture of the strata uplifts and underlying igneous intrusions.

Figure 6. Gravity modeling based on our velocity model. (a) Distribution of gravity anomalies and locations of the OBS stations. (b) The (red) calculated and (blue) observed gravity anomalies. (c) The obtained density model. The bodies with a density of 3.0 g/cm^3 reflect the HVBs.

Figure 7. (a) The background velocity model for the synthetic tests. (b) Input model of a checkerboard resolution test. The input amplitudes of velocity perturbations are 5%. (c) The result of the checkerboard resolution test, which shows that the pattern and amplitudes of the input velocity anomalies are well recovered. The grid interval is 20 km in the horizontal direction and 10 km in depth. (d) Input model for a synthetic recovery test for checking the reliability of HVBs in the lower crust. (e) Output result which indicates that the HVBs can be revealed by the tomographic inversion of our data set.

Figure 8. (a) Distribution of standard deviations of P-wave velocity and Moho depth obtained by using a Monte Carlo method with 100 random starting models. Green dotted lines show locations of 100 starting Moho depths. Red dotted lines show the inverted results of the Moho depth, indicating that the Moho depth can be well determined in areas with good ray coverage. (b) RMS travel-time residuals for the 100 starting velocity models. (d) RMS travel-time residuals for the 100 inverted velocity models.

Figure 9. Examples of sills, volcanic bodies and lava flows identified from the multichannel reflection seismic data. Locations of the four profiles (a-d) are shown in Figure 1b.

Figure 10. Spatial distributions of the volcanic seamounts, sills and lava flows, and lower crustal HVBs. The ellipses in the upper image denote the submarine volcanic seamounts revealed by Fan et al. (2017). The red shadows in the middle image show locations of sills and lava flows, which are identified from the multichannel reflection seismic profiles located in Figure 1b. Examples of the sills are shown in Figures 5 and 8. The thickness distribution of lower crustal HVBs in the lower image is constructed by integrating the present and previous results (Nissen et al., 1995; Yan et al., 2001; Wang et al., 2006; Wei et al., 2011; Lester et al., 2014).

Figure 11. A multi-level movement model of magmatic plumbing system. The orange shadow denotes a low-velocity anomaly in the upper mantle revealed by Xia et al. (2016). The thick black line denotes the lithosphere-asthenosphere boundary (LAB) derived from the results of Tang and Zheng (2013). Magma from the upper mantle intruded into the lower crust and formed the crustal reservoirs (red shadows in the lower crust) which fed the overlying sills and dikes (green shadows in the crust). The extensional faults (black dashed lines) developed at the rifting stage served as conduits for the magmatic upward migration. The igneous intrusions (vertical arrows and red dashed lines) could induce the forced folds of strata (black curves).

Figure 1

Figure 2

(a)

(b)
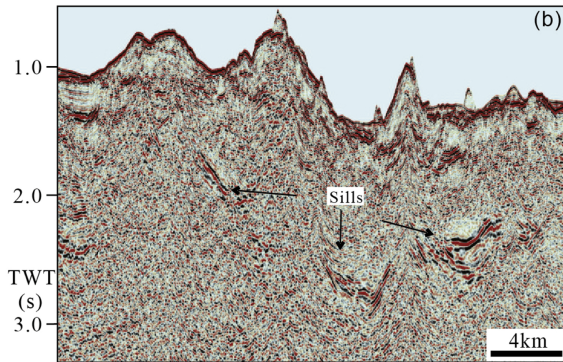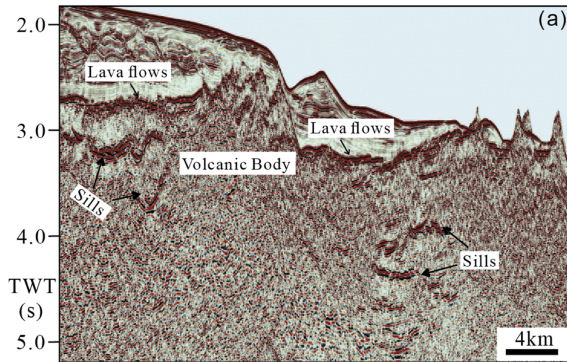
Final RMS = 0.085 (s)

(c)

(d)
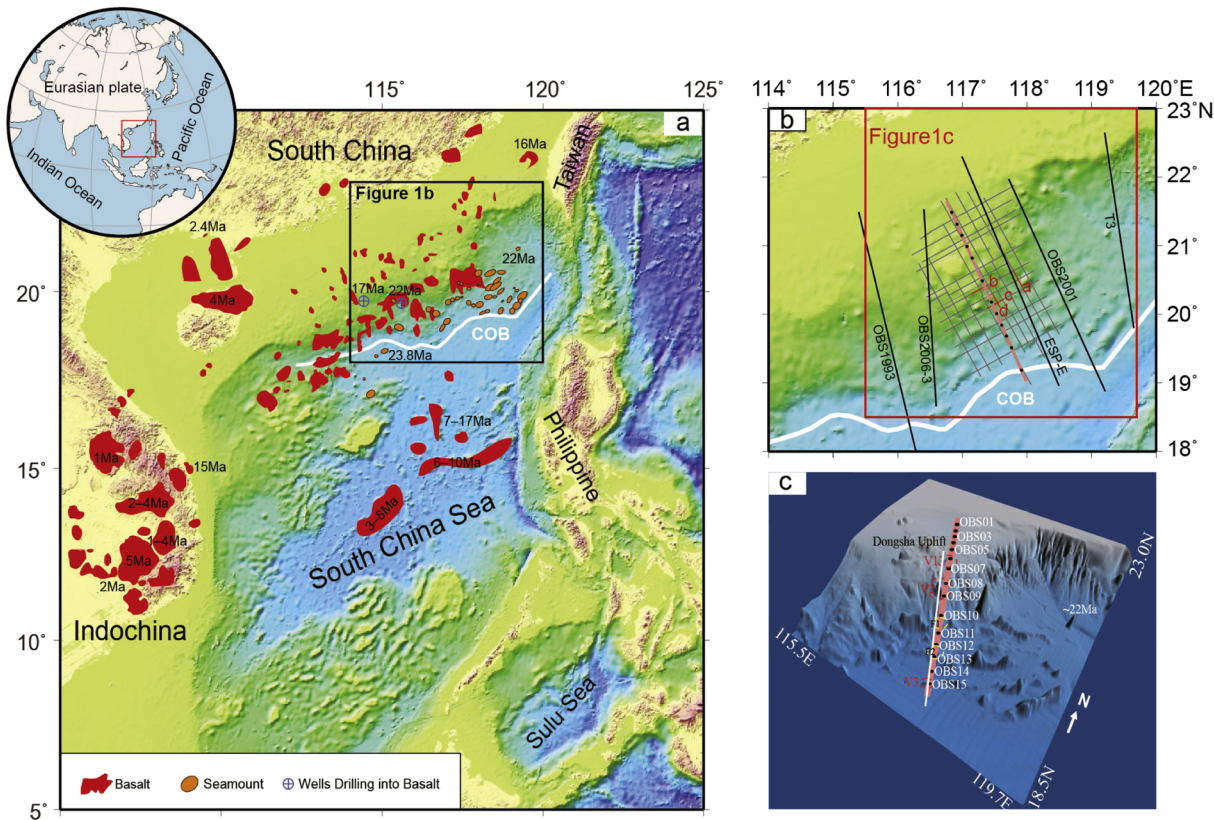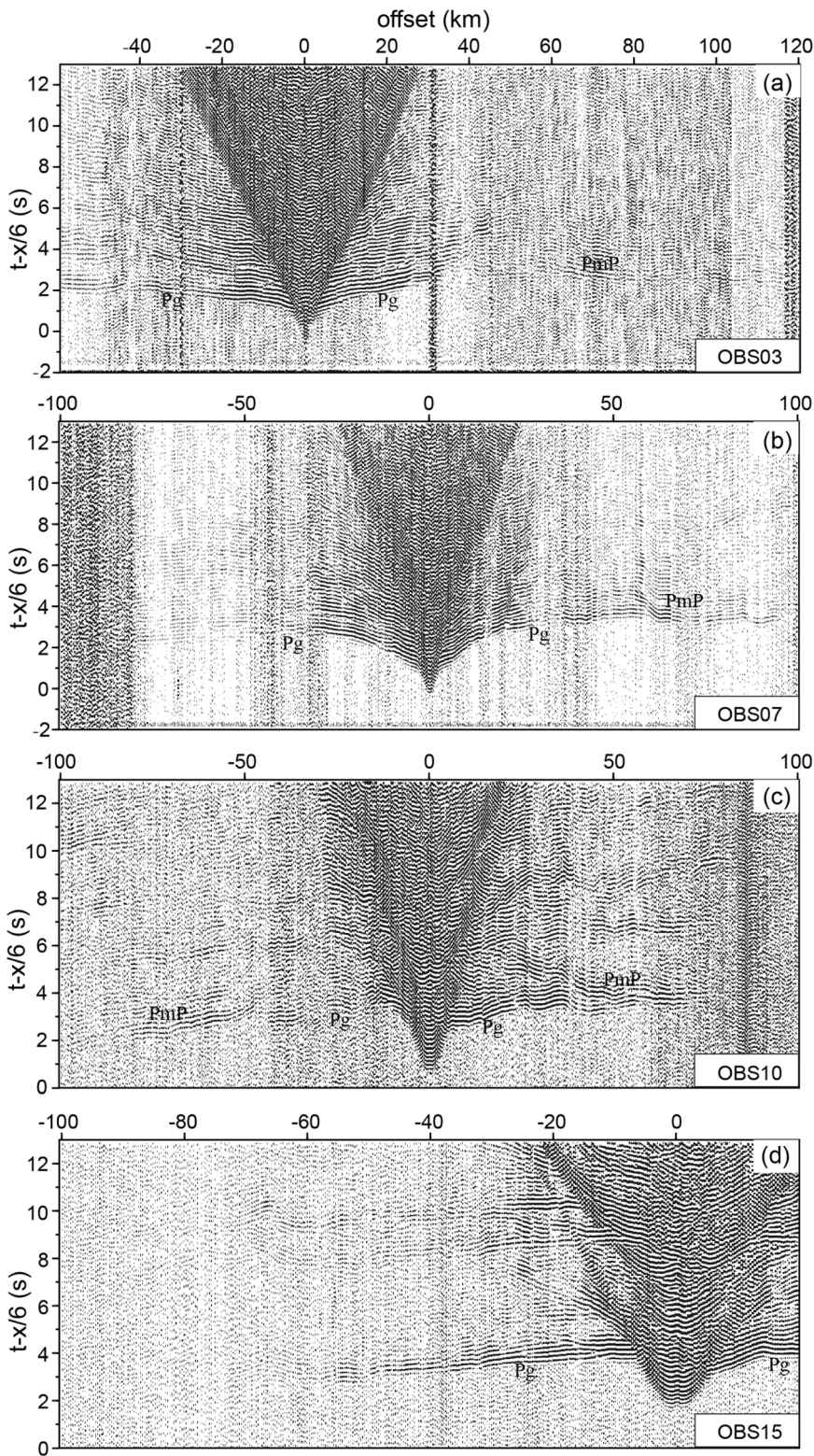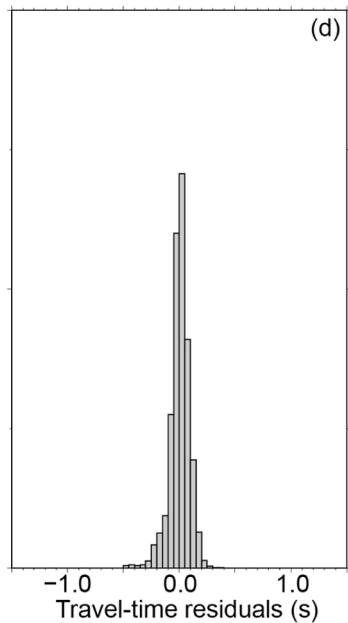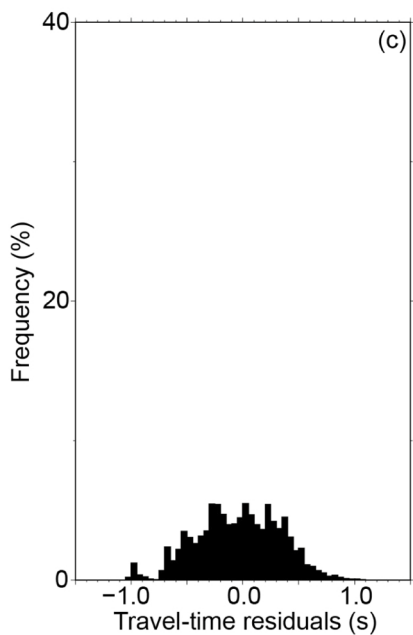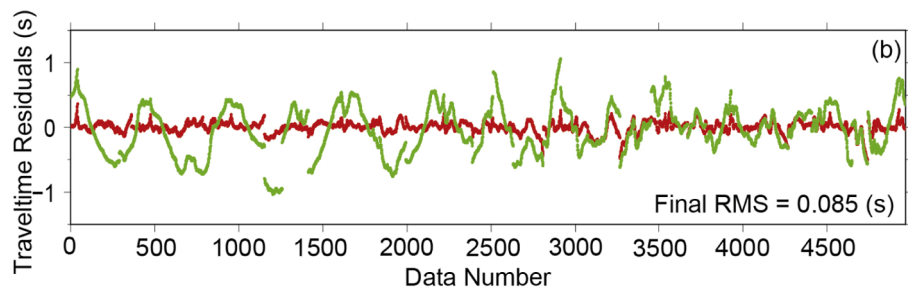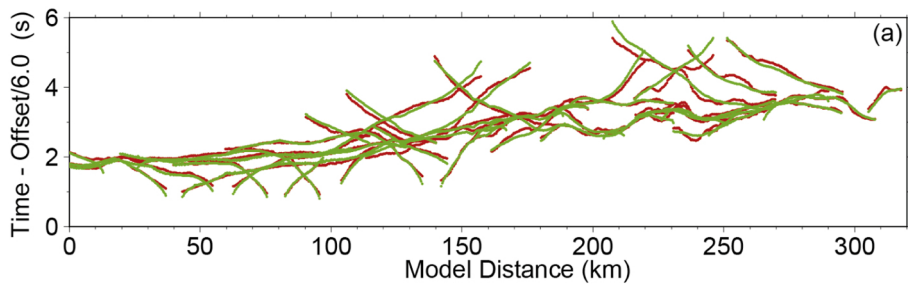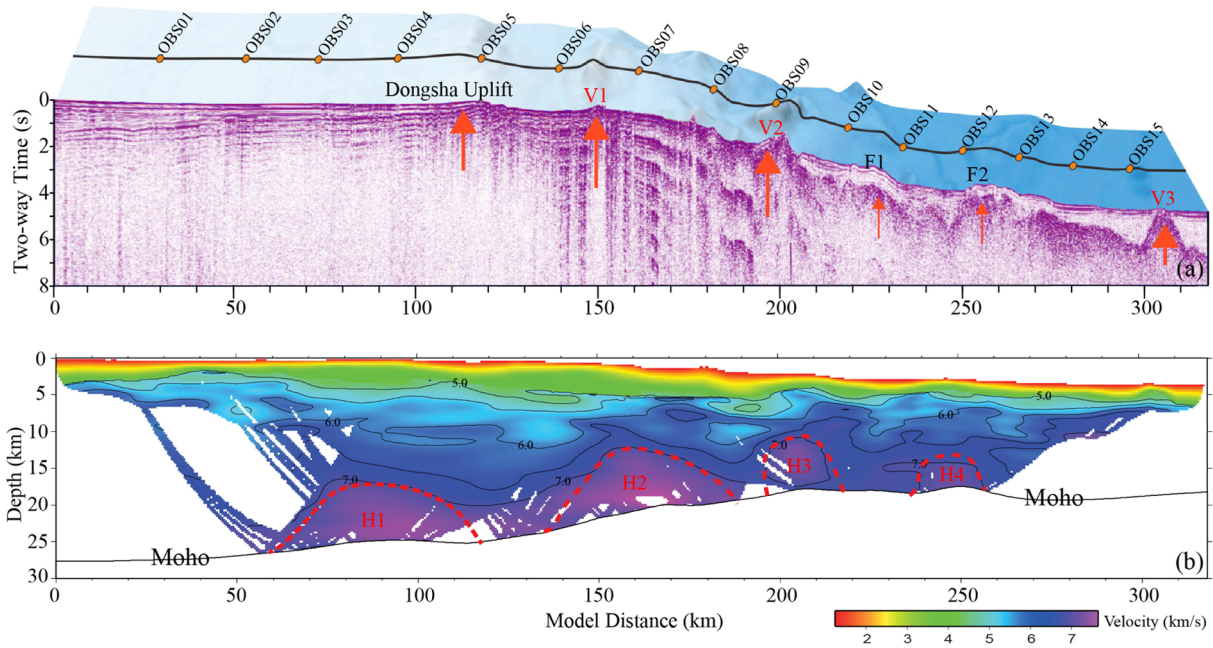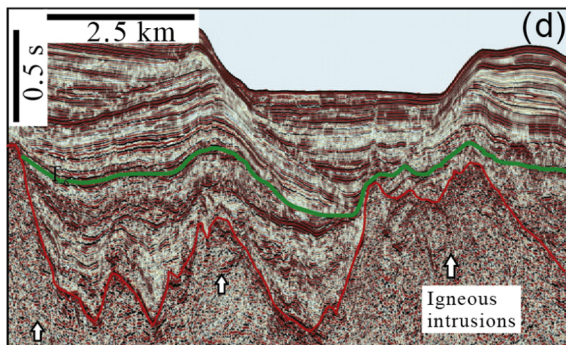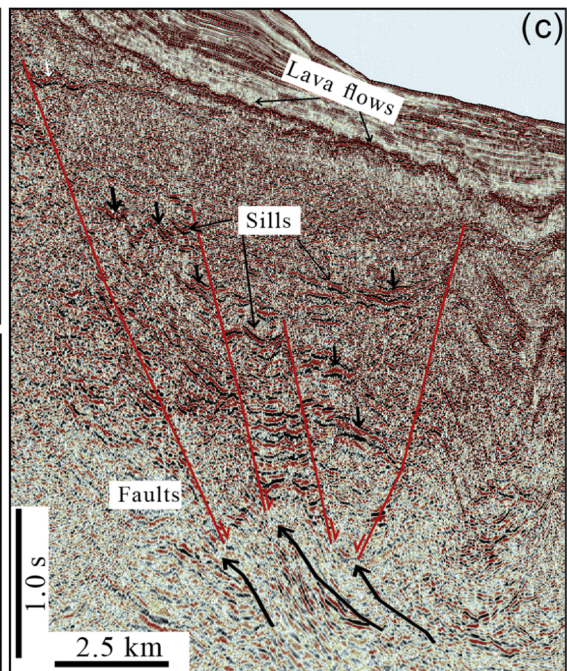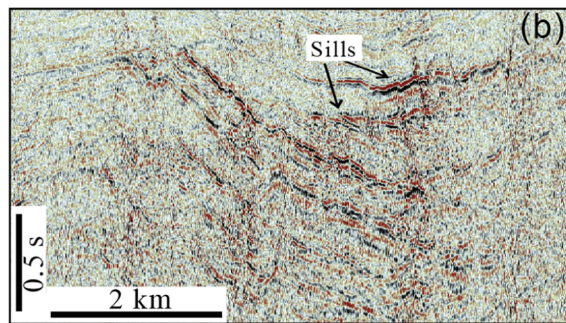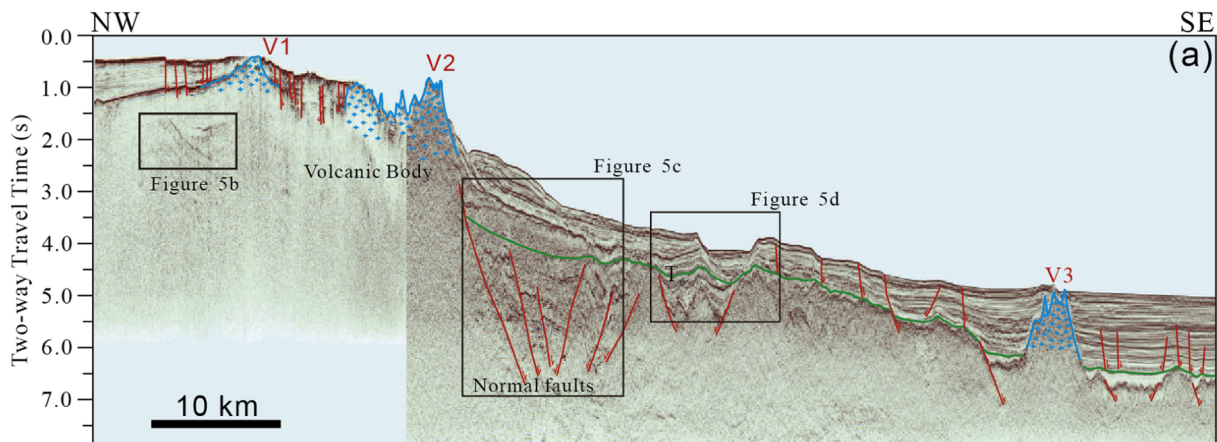
Figure 3

Figure 4

Figure 5
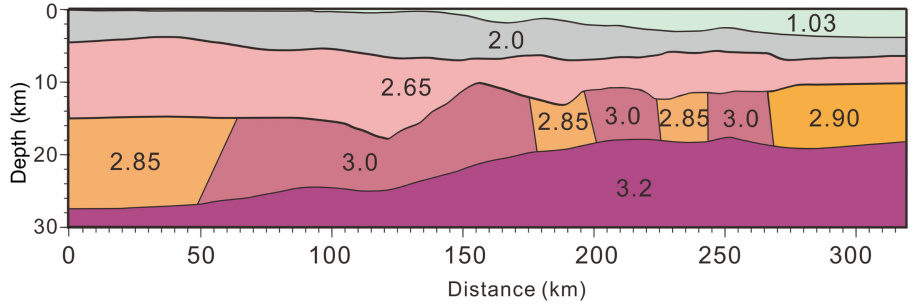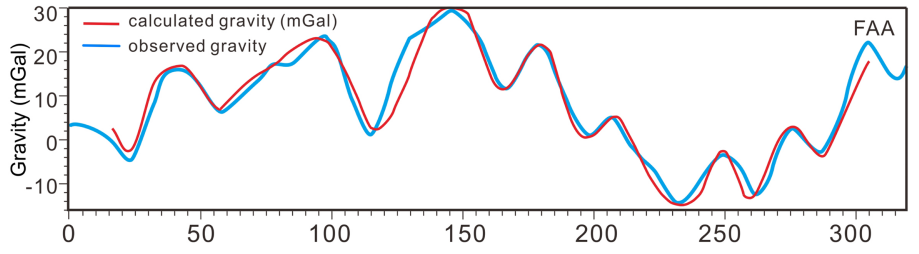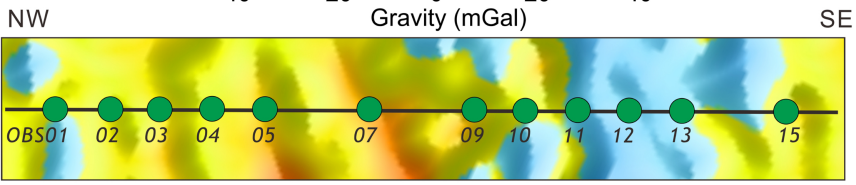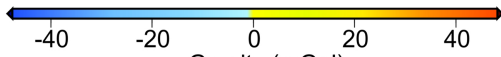
Figure 6
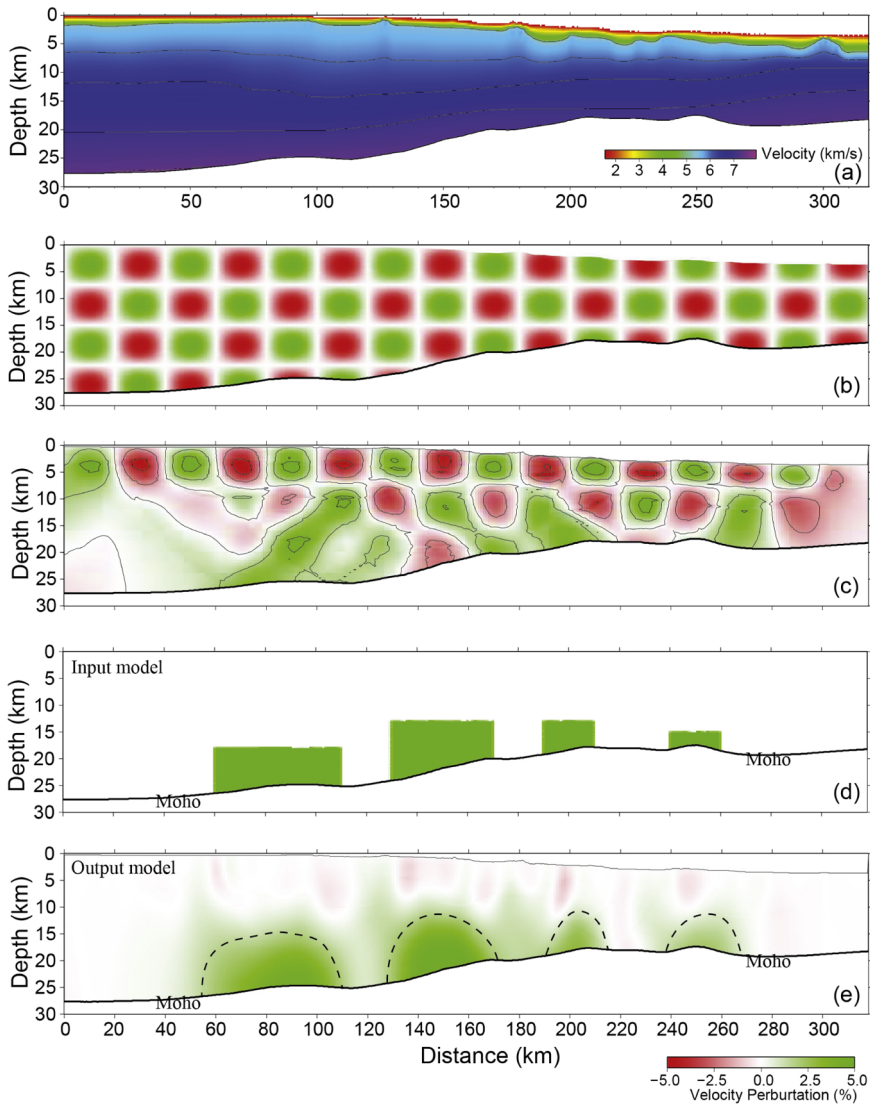
Figure 7
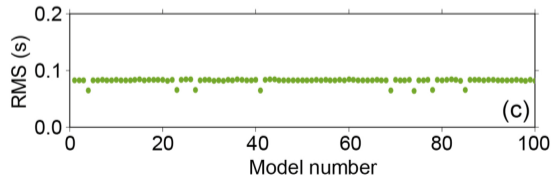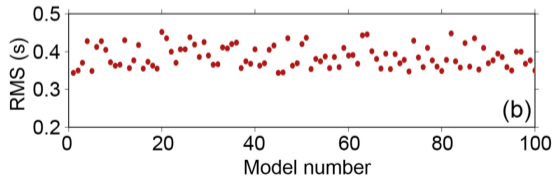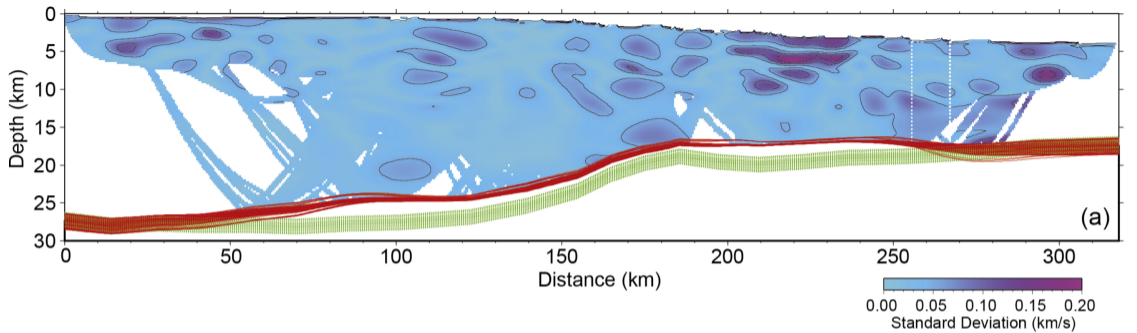
Figure 8
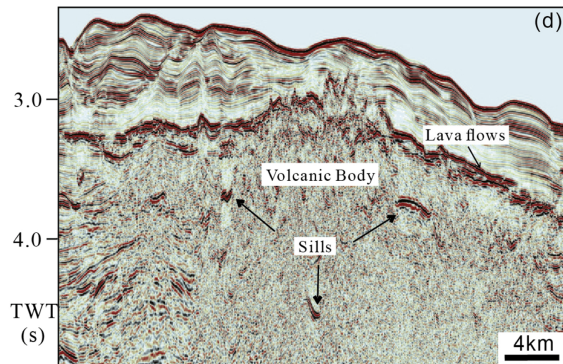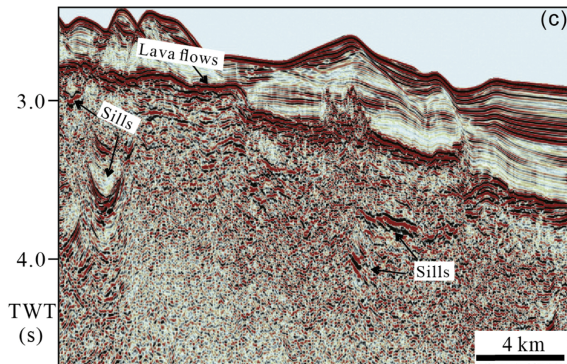
Figure 9

Figure 10

Figure 11